Electron Spin Resonance of Single Molecules and Magnetic Interaction through Ligands

Xue Zhang
Center for Quantum Nanoscience, IBS and Ewha Womans University
Christoph Wolf
Center for Quantum Nanoscience, IBS and Ewha Womans University
Yu Wang
Center for Quantum Nanoscience, IBS and Ewha Womans University
Hervé Aubin
Universités Paris-Saclay, CNRS, Centre de Nanosciences et de Nanotechnologies
Tobias Bilgeri
Institute of Physics, École Polytechnique Fédérale de Lausanne
Philip Willke
Center for Quantum Nanoscience, IBS and Ewha Womans University and Karlsruhe Institute of Technology
Andreas Heinrich
Institute of Basic Science at Ewha Womans University https://orcid.org/0000-0001-6204-471X
Taeyoung Choi (choi.taeyoung@qns.science)
Center for Quantum Nanoscience, IBS and Department of Physics, Ewha Womans University

Article

Keywords: Electron spin resonance (ESR) spectroscopy, magnetic interaction

Posted Date: February 2nd, 2021

DOI: https://doi.org/10.21203/rs.3.rs-134144/v1

Version of Record: A version of this preprint was published at Nature Chemistry on November 11th, 2021.
See the published version at https://doi.org/10.1038/s41557-021-00827-7.

Electron Spin Resonance of Single Molecules and Magnetic Interaction through Ligands

Xue Zhang[1,2], Christoph Wolf[1,2], Yu Wang[1,2], Hervé Aubin[3], Tobias Bilgeri[4], Philip Willke[1,2,5], Andreas J. Heinrich[1,6]* and Taeyoung Choi[1,6]*

1 Center for Quantum Nanoscience, Institute for Basic Science (IBS), Seoul 03760, Republic of Korea

2 Ewha Womans University, Seoul 03760, Republic of Korea

3 Universités Paris-Saclay, CNRS, Centre de Nanosciences et de Nanotechnologies, 91120, Palaiseau, France

4 Institute of Physics, École Polytechnique Fédérale de Lausanne, Station 3, CH-1015 Lausanne, Switzerland

5 Karlsruhe Institute of Technology, Karlsruhe 76131, Germany

6 Department of Physics, Ewha Womans University, Seoul 03760, Republic of Korea

Abstract

Electron spin resonance (ESR) spectroscopy is a crucial tool to determine the chemical structure of materials. ESR spectra measured in molecular systems, however, are established on large ensembles of spins and usually require complicated structural analysis. Recently, scanning tunneling microscopy (STM) combined with ESR has been proven as a powerful tool to image and coherently control individual atomic spins on surfaces. Here, we extend this technique to demonstrate ESR on single organic molecules - iron phthalocyanine (FePc) - and investigate the magnetic interactions between a molecular spin and either another molecular or atomic spin. We show that the molecular spin density is not only localized at the central Fe atom, but also distributed to the outer ligands, yielding a strongly anisotropic exchange coupling. Our work opens the door for using molecules in nanoscale ESR studies and promises tuning magnetic interactions between non-localized spins via tailoring ligand field symmetry and strength, which is essential for developing molecule-based spintronic devices.

Introduction (Main)

Chemical engineering and fabrication of single molecular spins at the nanoscale is of vital importance in molecule-based quantum devices.[1] To detect and drive single molecular spins, there have been various approaches such as optical detection of diluted molecular spins[2-4], magnetic resonance force microscopy[5], nitrogen-vacancy magnetometry[6], and break junction-based molecular devices[7-9]. Nevertheless, these systems may be subject to imbedding the molecule in a solid-state host and lack the flexibility to locate and access individual spins or harness intra- and inter-molecular spin-spin interactions.

The conventional electron spin resonance (ESR) studies on chemical ensembles[10,11] rely on the order of 10^{10} spins and often require complementary analysis techniques or theoretical calculations to elucidate the chemical structure at the molecular level. Development of scanning tunneling microscopy (STM) combined with ESR provides the advantage to investigate single molecular spins with atomic resolution. ESR-STM introduces a radio frequency (rf) electric field at the tunneling junction which can coherently drive individual atomic spins on surfaces[12-14]. The change in spin state is read out by a spin-polarized tip through tunneling magnetoresistance. The ESR-STM enables precise atom manipulation and imaging in sub-nanometer scale with sub-microelectronvolt (~10 MHz) energy resolution. Previous ESR-STM studies have focused on the spins of single transition metal adatoms[12,14-16] while reproducible ESR-STM results on molecules have not been reported to date, besides early attempts at room temperature and in ambient condition[17]. Molecules often have non-trivial spin distribution owing to the conjoint ligands[18], giving the unique opportunity to harness the spin distribution on the ligands for engineering spin-spin interaction with atomic resolution.

Metal phthalocyanines with various substitutional central metal atoms have been extensively employed as model systems in many-body quantum physics[18,19] and spin-dependent transport[20]. Here, we report a system of spin-1/2 molecules, iron phthalocyanine (FePc) on bilayer magnesium oxide (MgO) grown atop an Ag(100) surface. We perform ESR on individual FePc molecules and characterize the effects of ligand orientations on spin-spin interactions in FePc-FePc dimers and FePc-titanium atom (Ti) dimers. DFT calculations show that the spin density spreads to the outer molecular ligands. Our result highlights the role of non-localized spins in the transfer of magnetic interactions, which can be crucial for fabricating molecular devices[21].

Results and discussion

Individual FePc molecules, Fe, and Ti atoms were deposited subsequently onto a two monolayers (ML) MgO surface on Ag(100) substrate and all measurements were performed at a temperature of 2 K in a commercial STM with vector magnetic fields. The molecules and atoms are well isolated from each other at a low coverage and can be distinguished readily by their topographical appearance, as shown in Fig. 1a. Individual FePc molecules appear as a cross-like shape and lattice analysis indicates that the central Fe atom of the molecule sits atop an oxygen atom of MgO. The molecular axes are rotated by approximately 27° with respect to the underlying oxygen rows (inset of Fig. 1a). The Ti atoms in our experiment are mainly found on oxygen-oxygen bridge sites (marked as Ti_B) and appear taller than the Fe atoms atop the oxygen-site[22,23].

Previous studies have reported that FePc possesses a spin $S = 1$ in bulk and on several surfaces[24,25]. Surprisingly, our differential conductance (dI/dV) spectra measured on well-isolated FePc molecules on a MgO surface show a clear conductance maximum, reminiscent of the Kondo effect at zero bias when no magnetic field is applied, suggesting the FePc spin being $S = 1/2$

(Supplementary Fig. S1). This agrees with our DFT calculations, suggesting that an electron is transferred from the Ag substrate to the dz^2 orbital of FePc and the molecular spin becomes S = 1/2. The spin density of a negatively charged FePc (referred as FePc throughout this paper) is plotted in Fig. 1b, indicating that the spin distributes mainly on the central Fe atom and partially extends along the ligands[19]. Further analysis of the frontier orbital indicates that it consists of about 90% dz^2 and 10% contributions from the ligands (Supplementary Information Section 8).

We performed ESR on individual FePc molecules using rf frequency sweeps[12,14] at a fixed external magnetic field (Fig. 1c). The external magnetic field sets the Zeeman splitting of the FePc spin and the two Zeeman states of FePc spin (labeled as $|0\rangle$ and $|1\rangle$) can be coherently driven when the frequency of the applied oscillating electric field V_{rf} matches the Larmor frequency (inset of Fig. 1c). The spin Hamiltonian of a single FePc spin system can be written as:

$$H_0 = 2\mu_{\mathrm{FePc}}\boldsymbol{B}\cdot\boldsymbol{S}, \qquad (1)$$

where μ_{FePc} is the magnetic moment of FePc. $\boldsymbol{S}$ is the spin operator and the total magnetic field $\boldsymbol{B}$ which sets the Zeeman splitting is a sum of external magnetic field ($\boldsymbol{B}_{\mathrm{ex}}$) and tip field ($\boldsymbol{B}_{\mathrm{tip}}$): $\boldsymbol{B} = \boldsymbol{B}_{\mathrm{ex}} + \boldsymbol{B}_{\mathrm{tip}}$. When we apply an external magnetic field along the out-of-plane (z) direction, we simplify the external magnetic field and tip field as B_{z} and B_{tip}. The resonance frequency f_0 corresponding to the transition between $|0\rangle$ and $|1\rangle$ states is determined by

$$hf_0 = 2\mu_{\mathrm{FePc}}(B_{\mathrm{z}} + B_{\mathrm{tip}}). \qquad (2)$$

As shown in Fig. 1c and d, f_0 of a single FePc molecule shifts linearly to lower frequencies as the set tunneling current (I_{set}) increases at fixed DC bias (V) and B_z, indicating that the tip field (B_{tip}) is proportional to I_{set}[26,27] and opposite to the external magnetic field direction. This holds for all the tips used throughout this paper. In Fig. 1d, the vertical intercept, which is determined by

extrapolating the curve of f_0 vs I_{set} to zero B_{tip} (I_{set}), corresponds to the Zeeman splitting in the absence of a tip magnetic field. We can thus extract the magnetic moment of an individual FePc molecule (μ_{FePc}), 1.058±0.003 μ_{B}, free from the influence of any tip field. For a given tip at each set tunneling current, B_{tip} can be calculated precisely by using $B_{\mathrm{z}} - \frac{hf_0}{2\mu_{\mathrm{FePc}}}$ where the fitted μ_{FePc} is used, as shown by the double x-axes of Fig. 1d. We also found that the magnetic moment extracted from varied external fields at a fixed tip field gives consistent FePc magnetic moment of approximately 1 μ_{B} and obtained an averaged μ_{FePc} of 1.028±0.023 μ_{B} by measuring 14 individual FePc molecules (Supplementary Fig. S3). Moreover, we noted that μ_{FePc} differed by approximately 5% in two different directions of magnetic field (i.e. B_{x} and B_{z}, Supplementary Fig. S2). Such deviation may stem from the spin occupied orbital configuration. These results imply that the magnetic moment of FePc on MgO is nearly isotropic having spin-1/2 and the tip field can be utilized as a local magnetic field addressing an individual spin.

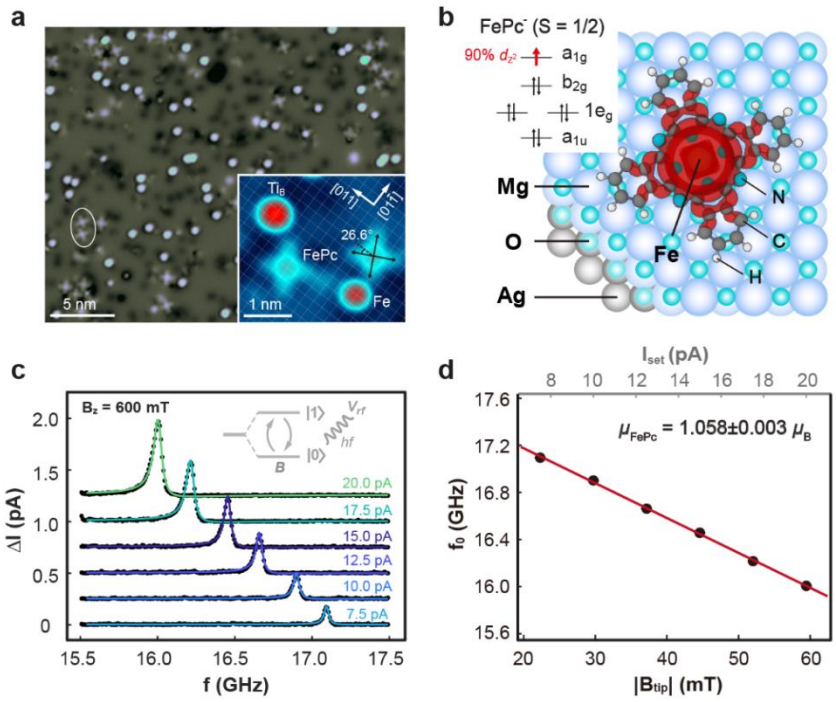

Fig. 1 | FePc molecules adsorbed on MgO/Ag(100) and ESR measurements with varied tip fields. a, STM

images of FePc molecules, Fe, and Ti_B atoms adsorbed on MgO surface. The white circle indicates a naturally formed FePc-FePc dimer. The white grids in the inset indicate oxygen sites of the underlying MgO surface throughout this paper. Black arrows describe the molecular axes pointing to the benzene rings. Scanning conditions: V = 200 mV, I_{set} = 12 pA for bigger image and I_{set} = 10 pA for the inset. **b,** Isosurface representation of the frontier orbital (isovalue: 10^{-5}) corresponding to the molecular frontier orbital (a_{1g} in the inset). Top left Inset: electron occupancy of molecular frontier orbitals. **c,** ESR spectra of an individual FePc molecule measured at different tunneling currents. ESR conditions: V = 100 mV, V_{rf} = 10 mV. Each spectrum is shifted vertically from one another by 0.75 pA for clarity. Colored lines are Lorentzian fits of raw ESR spectra (black dots). Inset: sketch of driving electron spin resonance in a two-level system with an rf electric field. **d,** Linear fit (red line) of resonance frequencies obtained from (**c**) as a function of B_{tip} (I_{set}).

To investigate the spin-spin interaction of the FePc molecular system, we performed ESR measurements on naturally formed FePc-FePc dimers (white circle in Fig. 1a). We define the configuration of a dimer as (m, n) by labeling the separation between the two Fe centers in the dimer in increments of the oxygen lattice along $[01\bar{1}]$ and [011], respectively. We found two dominant configurations, (3, 4) and (0, 5), which have the identical distance of 1.45 nm (given the MgO lattice constant: 0.29 nm) between the centers of the two molecules. When measuring on one of the FePc molecules in either dimer (3, 4) or (0, 5), we observed multiple ESR peaks as shown in Fig. 2b and e. For each dimer, the splitting between two adjacent ESR peaks appears to be independent of the tip field, implying the splitting is purely associated with the intermolecular coupling while the intensity of each peak evolves differently as the tip field varies (Fig. 2c and f). Moreover, the ESR splitting on (3, 4) and (0, 5) configurations is different although the center-center distance of the configurations is the same, which we will discuss later.

In order to understand the ESR spectra quantitatively, we utilize a Hamiltonian model of the two-spin system including exchange and dipolar coupling[28,29] between two FePc molecules:

$$H_{12} = 2\mu_1(\boldsymbol{B}_{\text{ex}} + \boldsymbol{B}_{\text{tip}}) \cdot \boldsymbol{S}_1 + 2\mu_2 \boldsymbol{B}_{\text{ex}} \cdot \boldsymbol{S}_2 + J\boldsymbol{S}_1 \cdot \boldsymbol{S}_2 + D[\boldsymbol{S}_1 \cdot \boldsymbol{S}_2 - \mathbf{3}(\boldsymbol{S}_1 \cdot \hat{\boldsymbol{r}})(\boldsymbol{S}_2 \cdot \hat{\boldsymbol{r}})]. \quad (3)$$

Here, the subscripts 1, 2 represent the two FePc spins in a dimer. The one under the tip is denoted as 1 whose Zeeman energy is set by both external magnetic field and tip field. The μ_1 and μ_2 are the magnetic moment of each FePc. The first two terms describe the Zeeman energy of a dimer system. Both FePc spins align with the external magnetic field direction since both molecules are spin-1/2 . The third and last term represent intermolecular exchange and dipolar coupling with the energy constant J and D, respectively. $\hat{\boldsymbol{r}}$ is the unit distance vector connecting the centers of two FePc spins. D is given by $\frac{\mu_0\mu_1\mu_2}{\pi r^3}$, where μ_0 is the vacuum permeability. The presence of J and D makes the quantum eigenstates deviate from the four pure Zeeman product states $|00\rangle$, $|01\rangle$, $|10\rangle$ and $|11\rangle$, giving rise to singlet-triplet states. While $|00\rangle$ and $|11\rangle$ remain as the eigenstates of H_{12}, the other two eigenstates become superpositions of the two Zeeman states $|01\rangle$ and $|10\rangle$ as defined below:

$$|-\rangle = -\frac{\alpha}{\sqrt{\alpha^2+1}}|01\rangle + \frac{1}{\sqrt{\alpha^2+1}}|10\rangle,$$

$$|+\rangle = \frac{1}{\sqrt{\alpha^2+1}}|01\rangle + \frac{\alpha}{\sqrt{\alpha^2+1}}|10\rangle$$

where α indicates the relative weight of $|01\rangle$, $|10\rangle$ component in the $|-\rangle$ and $|+\rangle$ states[22,28] and equals to $\frac{\delta+\sqrt{\varepsilon^2+\delta^2}}{\varepsilon}$, in which $\delta = 2(\mu_1 - \mu_2)B_{\text{ex}} + 2\mu_1 B_{\text{tip}}$ and $\varepsilon = J - \frac{D}{2}(1 - 3\cos^2\theta)$. θ is the angle between $\hat{\boldsymbol{r}}$ and FePc spin orientation. Figure 2g depicts a schematic diagram of eigenenergies for the given eigenstates $|00\rangle$, $|-\rangle$, $|+\rangle$ and $|11\rangle$ (denoted as E_{00}, E_-, E_+ and E_{11}) as a function of B_{ex} and B_{tip}. The four possible transitions between these states account for the ESR peaks shown in Fig. 2c and f, labeled as $f_1 = \frac{E_- - E_{00}}{h}$, $f_2 = \frac{E_{11} - E_+}{h}$, $f_3 = \frac{E_+ - E_{00}}{h}$, and $f_4 = \frac{E_{11} - E_-}{h}$, respectively. Fitted ESR transitions based on this singlet-triplet model (dotted white curves in Fig.

2c,f) show excellent agreement with the experimental data (Supplementary Information Section 5).

From the expression of α with δ, we note that the tip field can tune the relative weight of $|01\rangle$ and $|10\rangle$ in the $|-\rangle$ and $|+\rangle$ states at given B_{ex}, leading to different dominant ESR transitions at different tip fields (bold arrows in Fig. 2g at weak and strong tip fields). This accounts for the changes in the relative peak intensities of four ESR transitions. In particular, when B_{tip} is adjusted to achieve $\delta = 0$ (occurring at the avoided level crossing indicated by the dashed square in Fig. 2g) and $\alpha = 1$, meaning B_{tip} compensates the difference of Zeeman energy of two FePc spins (originated from the unequal magnetic moments), $|10\rangle$ and $|01\rangle$ are equally weighted in $|-\rangle$ and $|+\rangle$, f_1 and f_4 have the same intensity and f_2, f_3 merge to one peak (when $D \ll J$ and thus negligible), as indicated by the white arrows in Fig. 2c and f.

Using the above Hamiltonian model, we found that the ESR splitting Δf ($\Delta f = f_2 - f_1 = f_4 - f_3$) corresponds to the total coupling energy of the two-spin system,

$$\Delta f = J + D(1 - 3\cos^2\theta). \qquad (4)$$

Here, Δf depends on the angle between the external field and the sample plane due to an anisotropic dipolar distribution. We recorded Δf measured on a (3, 4) dimer with rotating external fields in order to differentiate the magnetic dipole interaction from the exchange interaction, as shown in Fig. 2h. By fitting to equation (4), we extracted J and D as 133±4 MHz and 16±3 MHz, respectively, which strongly suggests that the exchange coupling is the dominant interaction in the molecular spin pairs. The positive sign of J indicates that the coupling is antiferromagnetic (AFM). Moreover, we note that the measured dipolar coupling energy here is consistent with that expected from two ideal atomic spins having 1 μ_B with same center-center distance[22,28,29]. Based on this, we can extract the exchange coupling energy (J) of FePc dimers by subtracting the dipolar coupling

energy (D) of an atomic dimer with same center-center distance from the measured ESR splitting (Δf).

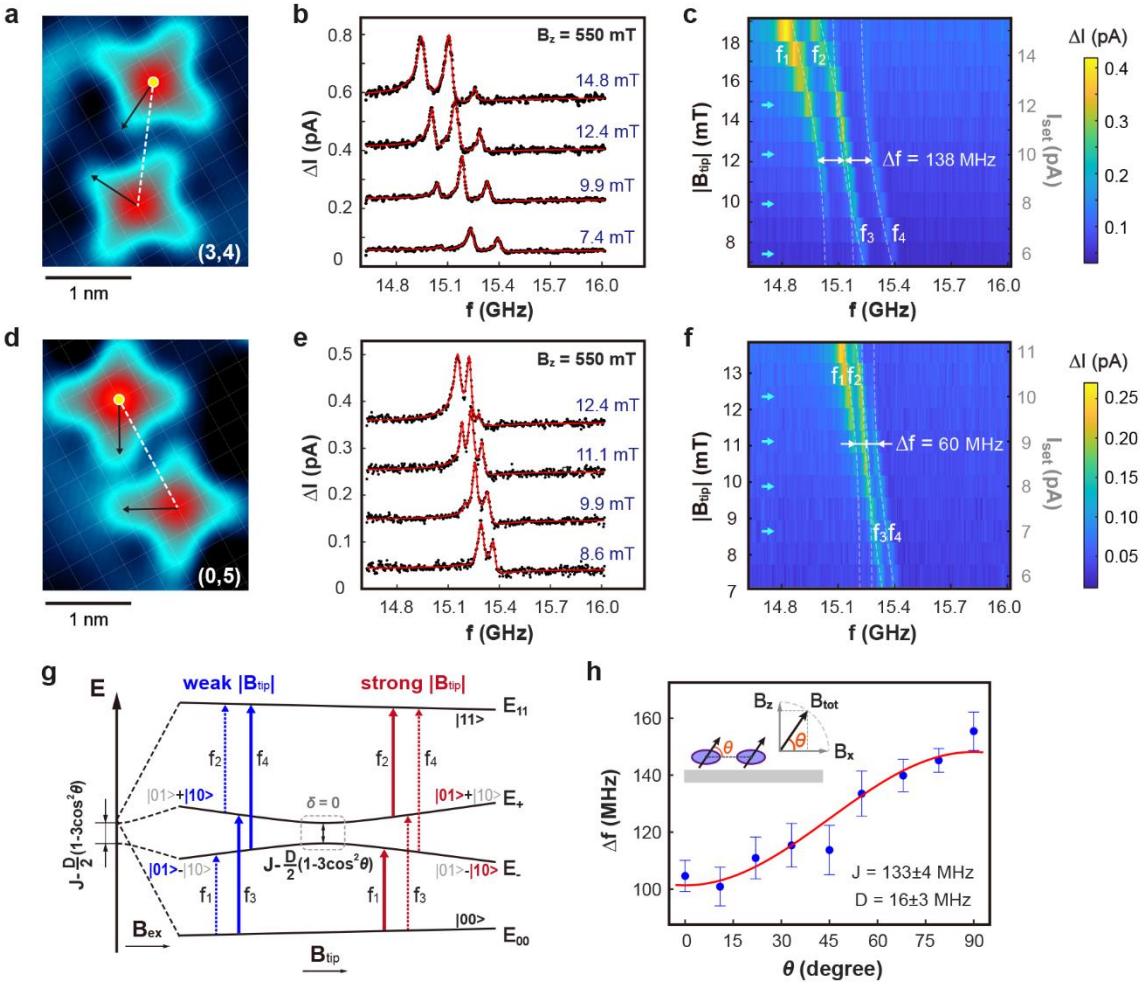

Fig. 2 | Spin coupling in FePc-FePc dimers. a, d, STM images of (3, 4) and (0, 5) dimer sharing the same center-center distance (dashed lines). Scanning conditions: V = 180 mV, I_{set} = 20 pA. **b, e,** Representative ESR spectra of the upper FePc measured at yellow dots in (**a**) and (**d**), respectively. **c, f,** ESR spectra plotted in color scale measured at different B_{tip} (I_{set}). Blue arrows indicate each ESR spectrum presented in (**b**) and (**e**). The dotted white curves represent fitted ESR transitions. **g,** Energy level diagram of a two-spin system considering exchange (J) and dipolar (D) interaction in the presence of B_{ex} and B_{tip}. **h**, Measured (blue dots) and fitted (red curve) ESR splitting Δf of a (3, 4) dimer while rotating the external field by θ with respect to the sample plane. Error bars denote the 95% confidence intervals. The total external field $|B_{\mathrm{tot}}|$ was kept at 550 mT during the

field rotation. All ESR spectra were taken with the same tip and V = 100 mV. (**a**)-(**f**) were obtained with an out-of-plane field of B_z = 550 mT. V_{rf} was set as 50 mV for (**b**)(**c**)(**h**) and 40 mV for (**e**)(**f**). ESR spectra of the lower FePc in each dimer are provided in Supplementary Fig. S4.

Previous ESR-STM studies on spin-spin interaction for atomic spins have shown that the exchange coupling is determined exclusively by the interatomic distance, implying that the atomic spin can be treated as a point magnet[22,28,29]. However, we found that the exchange coupling energy of (3, 4) and (0, 5) molecular dimer are different despite the same center-center distance. By measuring the ESR splitting (Δf) of approximately 20 dimers with B_z field only, we obtained a mean $\Delta\overline{f}$ of 134±19 MHz for the (3, 4) dimer while 64±7 MHz for the (0, 5) dimer (Supplementary Fig. S5). As mentioned above, the corresponding exchange coupling energy (J) extracted from $\Delta\overline{f}$ is 117±19 MHz and 47±7 MHz, respectively, by subtracting a dipole contribution of 17 MHz (calculated with two atomic spins having 1 μ_B for each). The non-negligible spin density on the outer ligands of the molecule may produce such a difference by generating additional coupling path for the intermolecular magnetic interaction. This implies that the distance between nearby ligands plays a crucial role in determining the magnetic coupling energy of molecular spin systems.

We performed DFT calculations to evaluate the influence of the ligand-ligand distance on the exchange coupling energy of FePc dimers. For both (3, 4) and (5, 0) dimers, the optimized adsorption configuration on a MgO surface was achieved when the two Fe centers are atop oxygen sites and the molecular lobes align along the (2, 1) lattice direction, in line with our STM topographic images. In subsequent calculations, we fixed one molecule in its optimized configuration (lower one in Fig. 3a) while rotating the other molecule (upper one in Fig. 3a) around its Fe center by an angle of ϕ with respect to the (2, 1) lattice direction. The center-center distance remains unchanged during such a rotation while the minimal ligand-ligand distance $d_{\min}$ (defined

as the nearest distance between two hydrogen atoms in the benzene rings as shown in Fig. 3c) changes accordingly. The variation in d_{min} when ϕ changes in (3, 4) and (5, 0) configuration is exhibited in the inset of Fig. 3b. We note a small difference in the d_{min} of (3, 4) and (5, 0) dimers when they are in optimized configurations (*i.e.* $\phi = 0°$). We then calculated the energy difference between ferromagnetic (E_{FM}) and antiferromagnetic coupling (E_{AFM}), the value of which equals to $\frac{1}{2}J$ for a two spin-1/2 system[30], as a function of d_{min} (Fig. 3b). The calculated $|E_{\mathrm{FM}} - E_{\mathrm{AFM}}|$ obeys an exponential decay ($\propto \exp(-d_{\mathrm{min}}/d)$) as d_{min} increases, which can be attributed to an exchange interaction through the molecular ligands. We extract a characteristic decay length of d = 0.0345 nm, which is similar to the length scale of exchange coupling in other molecular system[31]. The calculated J decreases as d_{min} gets larger in optimized (3, 4), (0, 5) and (2, 5) dimer configurations, consistent with the trend observed in our experiments (Fig. 3d). Besides, we found a few dimers whose ligand-ligand distance (Supplementary Fig. S7) deviated significantly from the optimized dimer configurations. The exchange coupling energy was significantly larger at equal center-center distance but shorter ligand-ligand distances. This result indicates that the molecular spin-spin coupling can be engineered via tuning inter-ligand symmetry.

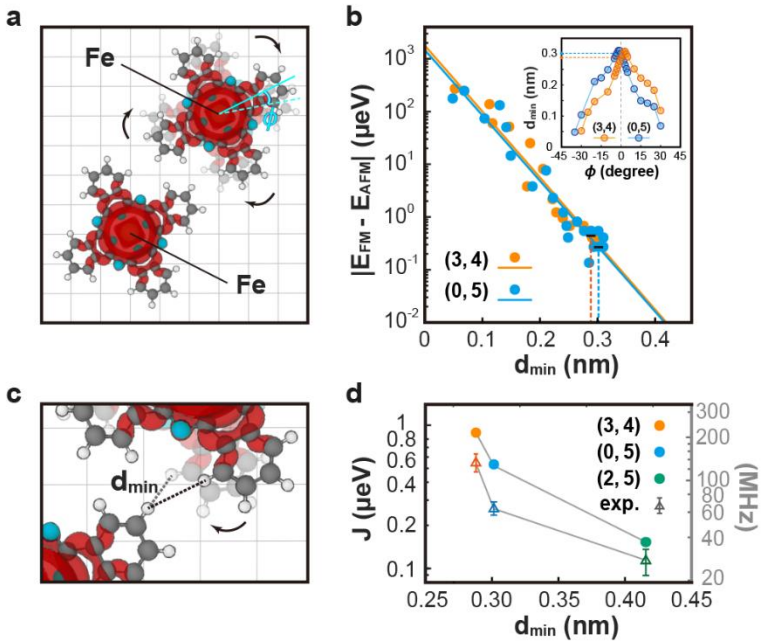

Fig. 3 | DFT calculations of exchange coupling in FePc-FePc dimer. a, Computational model of a FePc-FePc dimer. Fe-Fe distance is set according to experimental Fe coordinates. One molecule is fixed while the other one is rotated around the Fe center by ϕ. The minimum distance between two close-by ligands is denoted as d_{min} and amplified in (**c**). **b,** Calculated energy difference between FM and AFM coupling as a function of d_{min} for (3, 4) (orange dots) and (0, 5) (blue dots). Solid lines are fits based on $|E_{\mathrm{FM}} - E_{\mathrm{AFM}}| \propto \exp(-d_{\mathrm{min}}/d)$. Inset: d_{min}as a function of ϕ. The d_{min} of optimized (3, 4) and (0, 5) configurations and corresponding $|E_{\mathrm{FM}} - E_{\mathrm{AFM}}|$ are highlighted by dashed lines. **d,** Comparison of calculated (dots) and experimental (triangles) J for three different dimer configurations. The experimental data shown here is only the exchange coupling energy after subtracting the dipolar coupling energy (17 MHz for the (3, 4) , (0, 5) configurations and 14 MHz for the (2, 5) configuration) from the mean ESR splitting $\Delta\overline{f}$. Error bars represent the standard deviation. ESR spectra of (2, 5) dimer are provided in Supplementary Fig. S4.

To sense the spin distribution on the molecular ligands in greater detail, we substituted a spin-1/2 $\mathrm{Ti_B}$ atom for a FePc molecule and measured the exchange coupling energy in FePc-$\mathrm{Ti_B}$ pairs. While FePc-FePc dimers prefer to arrange only in a few configurations as mentioned above, the

relative spatial position of a Ti_B atom with respect to a FePc molecule can be controlled with atomic precision using atom manipulation. Here, the Ti_B atom is considered as a point magnet based on previous studies[28,29] and our DFT calculations (Supplementary Fig. S10). We applied only B_z field for measuring FePc-Ti_B pairs in order to be able to ignore the angular dependence of the dipolar interaction. The measured exchange coupling energy is thus merely its component along the out-of-plane direction, simplified as J. Figure 4a, c and e show three FePc-Ti_B pairs with the Ti_B atom sitting on different lattice sites: (3, 2.5), (3, 2.5) and (3.5, 1) with similar center-center (Fe-Ti_B) distances: 1.13 nm, 1.13 nm, and 1.06 nm. However, the relative angle between the connection of Fe-Ti_B and the molecular axes varies from 13.2° to 42.5°, corresponding to different Ti_B-ligand distances. As the angle becomes larger, i.e. the Ti_B is further away from the closest FePc ligand, we observed a drastic decrease in J by measuring ESR on FePc, as exhibited in Fig. 4b, d and f. Referring to the FePc-FePc dimer case, the J values shown here is the result after subtracting the dipolar coupling contribution (D) from the ESR splitting (Δf). The strong dependence on the relative Ti_B-ligand configuration of the exchange coupling energy indicates that the molecular ligands can influence the magnetic interaction significantly, which agrees with our measurements on FePc-FePc dimers.

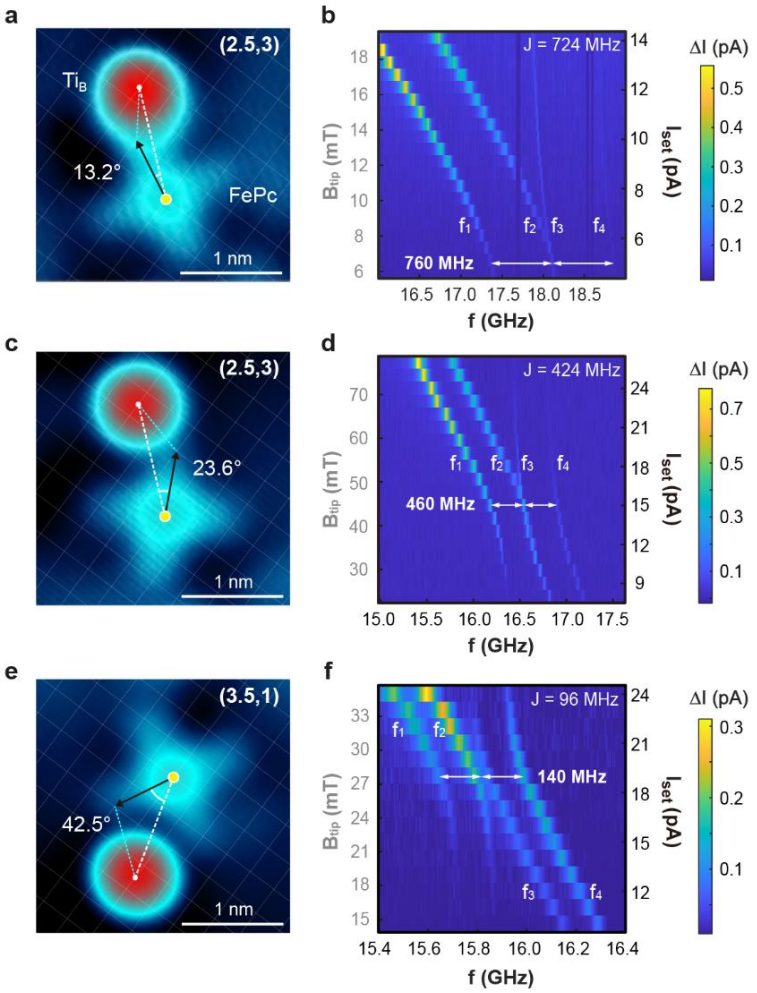

Fig. 4 | Exchange coupling of FePc-Ti$_B$ pairs with different Ti$_B$-ligand distance. a, c, e, STM images of three FePc-Ti$_B$ pairs with similar Fe-Ti$_B$ distance but different angle between molecular axes and the connection of Fe-Ti$_B$. Scanning conditions: (**a**) V = 200 mV, I_{set} = 6 pA; (**c**) V = 200 mV, I_{set} = 10 pA; (**e**) V = 150 mV, I_{set} = 20 pA. **b, d, f,** Respective ESR spectra measured on FePc (yellow spots in (**a**)(**c**)(**e**)) as a function of tip field by varying setpoint of the tunneling current. The exchange coupling energy J of each FePc-Ti$_B$ pair is labeled on the upper right corner, obtained by subtracting the dipolar coupling contribution (36 MHz for (2.5, 3) pair and 44 MHz for (3.5, 1) pair) from the measured ESR splitting. The external magnetic field was along out-of-plane direction for all FePc-Ti$_B$ measurements in our work. ESR conditions: V = 100 mV for all three pairs and (**b**) V_{rf} = 30 mV, B_z = 650 mT, (**d**) V_{rf} = 10 mV, B_z = 600 mT, (**f**) V_{rf} = 30 mV, B_z = 570 mT.

To map the anisotropic spin distribution of the FePc molecules, we measured J of a total of 14 FePc-Ti$_B$ pairs and observed a drastic decay of J as both Fe-Ti$_B$ distance (r) and ligand-Ti$_B$ distance (l) increases (Supplementary Fig. S8). Figure 5 (lower panel) displays the spatial map of J measured in different FePc-Ti$_B$ pairs. Considering the D_{4h} symmetry of the FePc molecule with respect to the MgO lattice, we duplicated the J of each pair to those equivalent adsorption sites. To emphasize the spin distribution on both Fe center and outer ligands, we utilized a heuristic model that simplified the entire spin distribution as two spin centers sitting at the central Fe atom and the nearest ligand, respectively. In this model, the J of a FePc-Ti$_B$ pair with the Ti$_B$ sitting at (r, l) with respect to the molecule can be described by a sum of two exponential functions, $J(r, l) = J_0(c_1 \cdot e^{-r/\lambda} + c_2 \cdot e^{-l/\lambda})$. Here, J_0 is the exchange coupling energy constant, which is assumed the same for Fe-Ti$_B$ interaction and ligand-Ti$_B$ interaction. c_1 and c_2 are fitting pre-factors. λ is the characteristic decay length toward the molecular center (Fe) and the ligand center, respectively. By choosing different lattice sites along the (2, 1) direction for determining l in the fitting, we note that c_1 and c_2 are optimized when the reference spot on the ligand is set at (1.42, 0.71), giving a ratio of $\frac{c_2}{c_1} = 0.03$ which is consistent with the 10% contribution of the spin density from the ligands (2.5% for each ligand). The characteristic decay length is fitted as λ = 0.0506 nm (see Supplementary Information Section 7 for more details). This allows us to approximate the spatial distribution of the exchange interaction with a molecule when the Ti$_B$ spin is positioned at different sites, as shown in the upper panel of Fig. 5. We found good agreement between this simple model and the experimental data by comparing the simulated contour lines with those measured data points, revealing the anisotropy of exchange interaction with a molecular spin. These results highlight that the ligands play a crucial role in molecular spin-spin interactions.

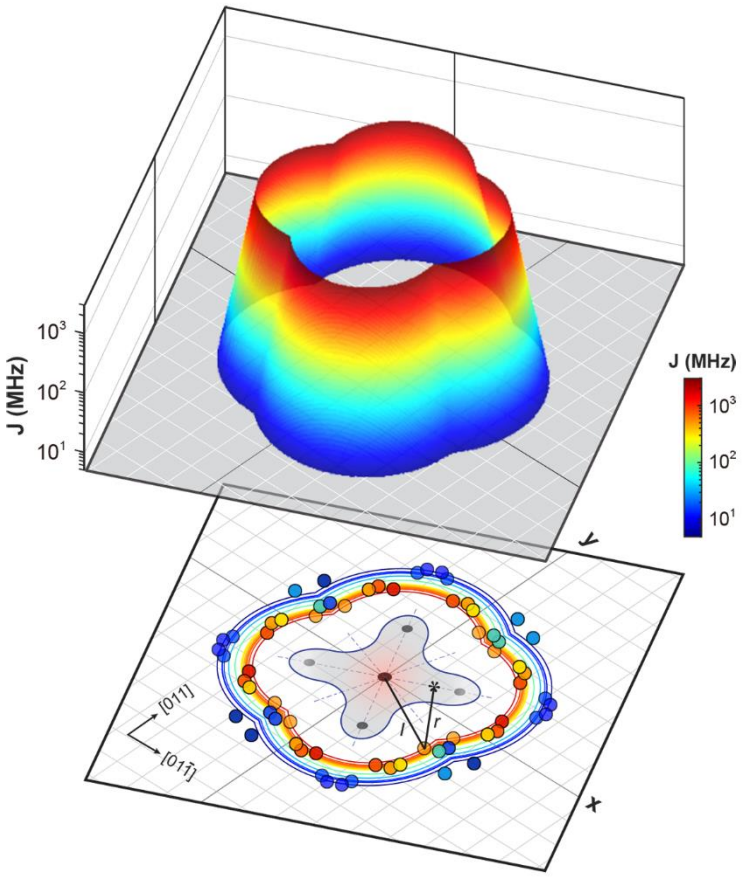

Fig. 5 | Anisotropic exchange coupling in FePc-Ti$_B$ pairs. Lower panel: measured J of different FePc-Ti$_B$ pairs expressed by colored dots and labelled at corresponding Ti$_B$ adsorption sites with respect to the central FePc model. In total, 14 pairs were measured and the data points corresponding to the measured J have been equivalently duplicated by a rotation and reflection process according to the molecular symmetry axes (dashed lines). The grey grids represent the oxygen lattice. J is the exchange coupling energy after subtracting the dipole contribution from the total ESR splitting. The contour lines are projected from the simulated spatial exchange coupling energy map choosing those J values obtained from the experiment. Upper panel: simulated spatial exchange coupling energy map by using a sum of two exponential terms representing r-dependence and l-dependence, respectively. The frequency range is set as 3,000 MHz (upper limit) and 5 MHz (lower limit).

Conclusions

We have demonstrated single-molecule ESR by driving the spin of an individual FePc molecule on a surface. ESR-STM measurements on molecular dimers and molecule-metal atom pairs enable us to investigate the crucial role of the molecular ligands on the exchange coupling between molecules. Here, we found that the magnetic exchange interaction with a molecule shows strong anisotropy, emphasizing the important role of ligands for the transfer of spin-polarization in molecular systems. Our work extends ESR-STM from single atoms to a much larger class of matter – magnetic molecules. This allows synthetic chemistry to design the spin properties through engineering the ligand field and symmetry. Moreover, our work suggests molecules as a potential platform to investigate magnetic interactions with non-localized spins, which has brought intensive interest in the field of metal-organic-networks and is essential for developing molecule-based spintronic and quantum information devices[32].

Methods

STM-ESR setup

ESR measurements were performed in a commercial low-temperature STM (Unisoku, USM1300). A radio frequency (rf) microwave which was generated by a signal generator (Keysight, E8257D) was added to a DC voltage (V) using a bias tee at the tip side. With this set-up, an oscillating electric field V_{rf} was applied at the tunneling junction[33]. The magnetic tip was prepared by transferring 3~5 Fe atoms from MgO surface to the tip apex and allowed a readout of the spin state by the spin-polarized tunneling current. During an ESR frequency sweep, the rf voltage and DC bias were applied continuously but the rf voltage was modulated at 95 Hz. The modulated tunneling current was then recorded by lock-in technique. All voltages in this paper are referred to the sample.

Sample preparation

Single crystalline Ag(100) was pretreated by alternative Ar^+ sputtering and annealing cycles. During MgO growth, Ag(100) was kept at 400°C and magnesium was evaporated onto clean Ag surface in an O_2 atmosphere of 1.1×10^{-6} torr. FePc was first deposited onto the MgO surface while the sample was kept at room temperature. The sample was then transferred to the cryostat for cooling down. Fe and Ti atoms were deposited subsequently onto the cold sample at 25-40 K. After the dosage of molecules and metal atoms, the sample was transferred to ~2 K environment for ESR measurements. The thickness of the MgO layer was determined by performing point-contact measurements on individual Fe atoms[34].

Titanium atom manipulation

After titanium deposition, naturally formed FePc-Ti_B pairs were abundant. In addition, we were able to position Ti_B atom using atom manipulation and construct FePc-Ti_B pairs with various configurations. When the tunneling conductance was set as $V \approx 350$ mV, $I \approx 2.2$ nA, the Ti_B atom under the tip could follow the tip movement and be positioned at desired sites. In contrast, controllable manipulation of FePc molecule rarely occurs under our manipulation parameters.

DFT calculations

All density functional theory (DFT) calculations were performed using Quantum Espresso (version 6.5) which implements DFT using plane waves and pseudopotentials[35,36]. Pseudopotentials were chosen based on the SSSP library and the basis set was expanded using a kinetic cutoff of 40 Rydberg[37]. All pseudopotentials use the generalized gradient approximation of Perdew, Burke and Ernzerhof (PBE) and we treated van der Waals interaction using Grimme's D3[38,39].

For single FePc, the calculation model includes 4 ML of silver capped by 2 ML of MgO exposing the (100) surface[40]. In z-direction, the cell is padded with 1.2 nm of vacuum. For FePc-FePc dimer, the cell was laterally expanded to accommodate both molecules and make sure that the separation of dimers and their periodic image is at least 5 times larger than the inter-dimer distance. The exchange coupling energy was calculated using the broken-symmetry approach introduced by Noodleman[30]. This approach maps the Kohn-Sham energies of the high-spin ($m_s = 1$) and the broken symmetry ($m_s = 0$) state to the diagonal elements of the Heisenberg Hamiltonian. More computational details can be found in Supplementary Information.

Supplementary information

(1) Kondo splitting in varied external magnetic fields.

(2) Extraction of μ_{FePc} by using different methods and in different magnetic fields.

(3) Statistics on magnetic moment of different individual FePc molecules.

(4) Current-dependence ESR spectra of different FePc-FePc dimers and statistics on coupling energy.

(5) ESR transitions in Heisenberg two-spin system with the tip field detuning effect.

(6) FePc-FePc dimers with closer ligand-ligand distance.

(7) Fitting of J as a function of $\mathrm{Ti_B}$-Fe distance and $\mathrm{Ti_B}$-ligand distance.

(8) Details of DFT calculations.

Acknowledgements

All authors acknowledge support from the Institute for Basic Science under grant IBS-R027-D1. We thank N. Lorente for fruitful discussions.

Contributions

T.C. and X.Z. designed the project. X.Z., Y.W., T.B. and P.W. performed the experiments. C.W. carried out DFT calculations. H.A. contributed to Hamiltonian model simulations. X.Z. and T.C. wrote the manuscript with help of all authors. T.C. and A.H. advised the project process.

Corresponding author

Correspondence to Andreas J. Heinrich (heinrich.andreas@qns.science) or Taeyoung Choi (choi.taeyoung@qns.science).

Competing interests

The authors declare no competing interest.

Data availability

All data that support the findings of this study are available in this manuscript and its Supplementary Information, or from the corresponding authors on reasonable request.

References

[1] Atzori, M. & Sessoli, R. The second quantum revolution: role and challenges of molecular chemistry. *J. Am. Chem. Soc.* **141,** 11339−11352 (2019).

[2] Wrachtrup, J., von Borczyskowski, C., Bernard, J., Orrit, M. & Brown, R. Optical detection of magnetic resonance in a single molecule. *Nature* **363,** 244–245 (1993).

[3] Köhler, J. et al. Magnetic resonance of a single molecular spin. *Nature* **363,** 242-244 (1993).

[4] Bayliss, S. L. et al. Optically addressable molecular spins for quantum information processing. *Science* **370**, 1309-1312 (2020).

[5] Rugar, D., Budakian, R., Mamin, H. J. & Chui, B. W. Single spin detection by magnetic resonance force microscopy. *Nature* **430,** 329–332 (2004).

[6] Lovchinsky, I. et al. Nuclear magnetic resonance detection and spectroscopy of single proteins using quantum logic. *Science* **351,** 836–841 (2016).

[7] Gehring, P., Thijssen, J. M. & van der Zant, H. S. J. Single-molecule quantum-transport phenomena in break junctions. *Nat. Rev. Phys.* **1,** 381–396 (2019).

[8] Vincent, R., Klyatskaya, S., Ruben, M., Wernsdorfer, W. & Balestro, F. Electronic read-out of a single nuclear spin using a molecular spin transistor. *Nature* **488,** 357–360 (2012).

[9] Thiele, S. et al. Electrically driven nuclear spin resonance in single-molecule magnets. *Science* **344,** 1135–1138 (2014).

[10] Tesi, L. et al. Quantum coherence in a processable vanadyl complex: new tools for the search of molecular spin qubits. *Chem. Sci.* **7,** 2074–2083 (2016).

[11] Graham, M. J. et al. Influence of electronic spin and spin-orbit coupling on decoherence in mononuclear transition metal complexes. *J. Am. Chem. Soc.* **136,** 7623–7626 (2014).

[12] Seifert, T. S. et al. Single-atom electron paramagnetic resonance in a scanning tunneling microscope driven by a radio-frequency antenna at 4 K. *Phys. Rev. Res.* **2,** 013032 (2020).

[13] Natterer, F. D. et al. Upgrade of a low-temperature scanning tunneling microscope for electron-spin resonance. *Rev. Sci. Instrum.* **90,** 013706 (2019).

[14] Baumann, S. et al. Electron paramagnetic resonance of individual atoms on a surface. *Science* **350,** 417–420 (2015).

[15] Willke, P. et al. Hyperfine interaction of individual atoms on a surface. *Science* **362,** 336–339

(2018).

[16] Yang, K. et al. Electrically controlled nuclear polarization of individual atoms. *Nat. Nanotechnol.* **13,** 1120–1125 (2018).

[17] Durkan, C. & Welland, M. E. Electronic spin detection in molecules using scanning-tunneling-microscopy-assisted electron-spin resonance. *Appl. Phys. Lett.* **80,** 458–460 (2002).

[18] Hiraoka, R. et al. Single-molecule quantum dot as a Kondo simulator. *Nat. Commun.* **8,** 16012 (2017).

[19] Mugarza, A. et al. Electronic and magnetic properties of molecule-metal interfaces: transition-metal phthalocyanines adsorbed on Ag(100). *Phys. Rev. B* **85,** 155437 (2012).

[20] Yang, K. et al. Tunable giant magnetoresistance in a single-molecule junction. *Nat. Commun.* **10,** 3599 (2019).

[21] Bogani, L. & Wernsdorfer, W. Molecular spintronics using single-molecule magnets. *Nat. Mater.* **7,** 179–186 (2008).

[22] Bae, Y. et al. Enhanced quantum coherence in exchange coupled spins via singlet-triplet transitions. *Sci. Adv.* **4,** eaau4159 (2018).

[23] Willke, P., Yang, K., Bae, Y., Heinrich, A. J. & Lutz, C. P. Magnetic resonance imaging of single atoms on a surface. *Nat. Phys.* **15,** 1005–1010 (2019).

[24] Tsukahara, N. et al. Adsorption-induced switching of magnetic anisotropy in a single iron(II) phthalocyanine molecule on an oxidized Cu(110) surface. *Phys. Rev. Lett.* **102,** 167203 (2009).

[25] Hiraoka, R. et al. Single-molecule quantum dot as a Kondo simulator. *Nat. Commun.* **8,** 16012 (2017).

[26] Yang, K. et al. Tuning the exchange bias on a single atom from 1 mT to 10 T. *Phys. Rev. Lett.* **122,** 227203 (2019).

[27] Yan, S., Choi, D.-J., Burgess, J. A. J., Rolf-Pissarczyk, S. & Loth, S. Control of quantum magnets by atomic exchange bias. *Nat. Nanotechnol.* **10,** 40–45 (2015).

[28] Yang, K. et al. Engineering the eigenstates of coupled spin-1/2 atoms on a surface. *Phys. Rev. Lett.* **119,** 227206 (2017).

[29] Choi, T. et al. Atomic-scale sensing of the magnetic dipolar field from single atoms. *Nat. Nanotechnol.* **12,** 420–424 (2017).

[30] Noodleman, L. Valence bond description of antiferromagnetic coupling in transition metal dimers. *J. Chem. Phys.* **74,** 5737–5743 (1981).

[31] Czap, G. et al. Probing and imaging spin interactions with a magnetic single-molecule sensor. *Science* **364,** 670–673 (2019).

[32] Ferrando-Soria, J. et al. A modular design of molecular qubits to implement universal quantum gates. *Nat. Commun.* **7,** 11377 (2016).

[33] Lado, J. L., Ferrón, A. & Fernández-Rossier, J. Exchange mechanism for electron paramagnetic resonance of individual adatoms. *Phys. Rev. B* **96,** 205420 (2017).

[34] Paul, W. et al. Control of the millisecond spin lifetime of an electrically probed atom. *Nat. Phys.* **13,** 403–407 (2017).

[35] Giannozzi, P. et al. QUANTUM ESPRESSO: a modular and open-source software project for quantum simulations of materials. *J. Phys. Condens. Matter* **21,** 395502 (2009).

[36] Giannozzi, P. et al. Advanced capabilities for materials modelling with Quantum ESPRESSO. *J. Phys. Condens. Matter* **29,** 465901 (2017).

[37] Prandini, G., Marrazzo, A., Castelli, I. E., Mounet, N. & Marzari, N. Precision and efficiency in solid-state pseudopotential calculations. *npj Comput. Mater.* **4,** 1–17 (2018).

[38] Perdew, J. P., Burke, K. & Ernzerhof, M. Generalized gradient approximation made simple.

Phys. Rev. Lett. **77,** 3865–3868 (1996).

[39] Grimme, S., Hansen, A., Brandenburg, J. G. & Bannwarth, C. Dispersion-corrected mean-field electronic structure methods. *Chem. Rev.* **116,** 5105–5154 (2016).

Figures

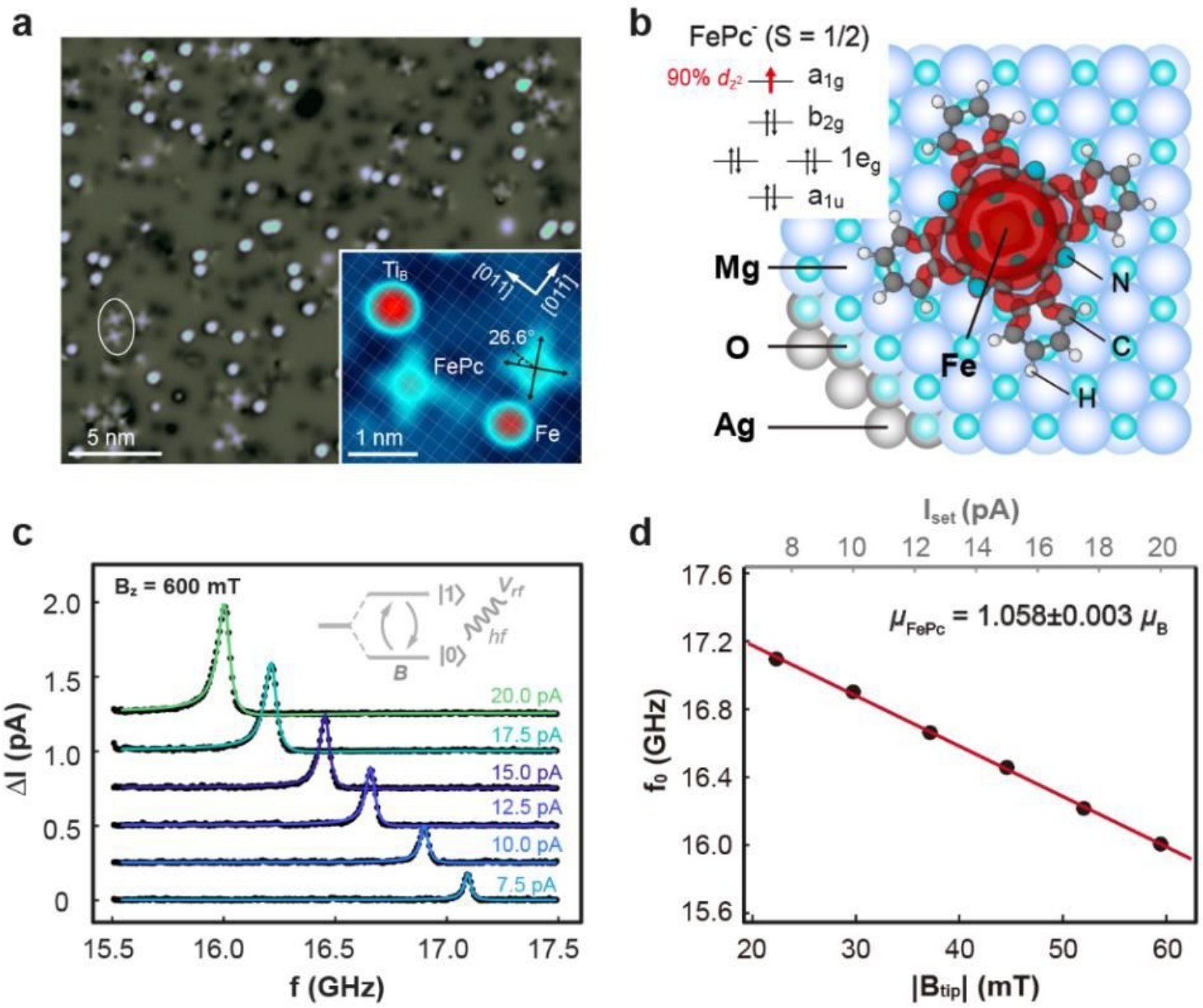

Figure 1

FePc molecules adsorbed on MgO/Ag(100) and ESR measurements with varied tip fields. a, STM images of FePc molecules, Fe, and TiB atoms adsorbed on MgO surface. The white circle indicates a naturally formed FePc-FePc dimer. The white grids in the inset indicate oxygen sites of the underlying MgO surface throughout this paper. Black arrows describe the molecular axes pointing to the benzene rings. Scanning conditions: V = 200 mV, Iset = 12 pA for bigger image and Iset = 10 pA for the inset. b, Isosurface representation of the frontier orbital (isovalue: 10-5) corresponding to the molecular frontier orbital (a1g in the inset). Top left Inset: electron occupancy of molecular frontier orbitals. c, ESR spectra of an individual FePc molecule measured at different tunneling currents. ESR conditions: V = 100 mV, Vrf = 10 mV. Each spectrum is shifted vertically from one another by 0.75 pA for clarity. Colored lines are

Lorentzian fits of raw ESR spectra (black dots). Inset: sketch of driving electron spin resonance in a two-level system with an rf electric field. d, Linear fit (red line) of resonance frequencies obtained from (c) as a function of Btip (Iset).

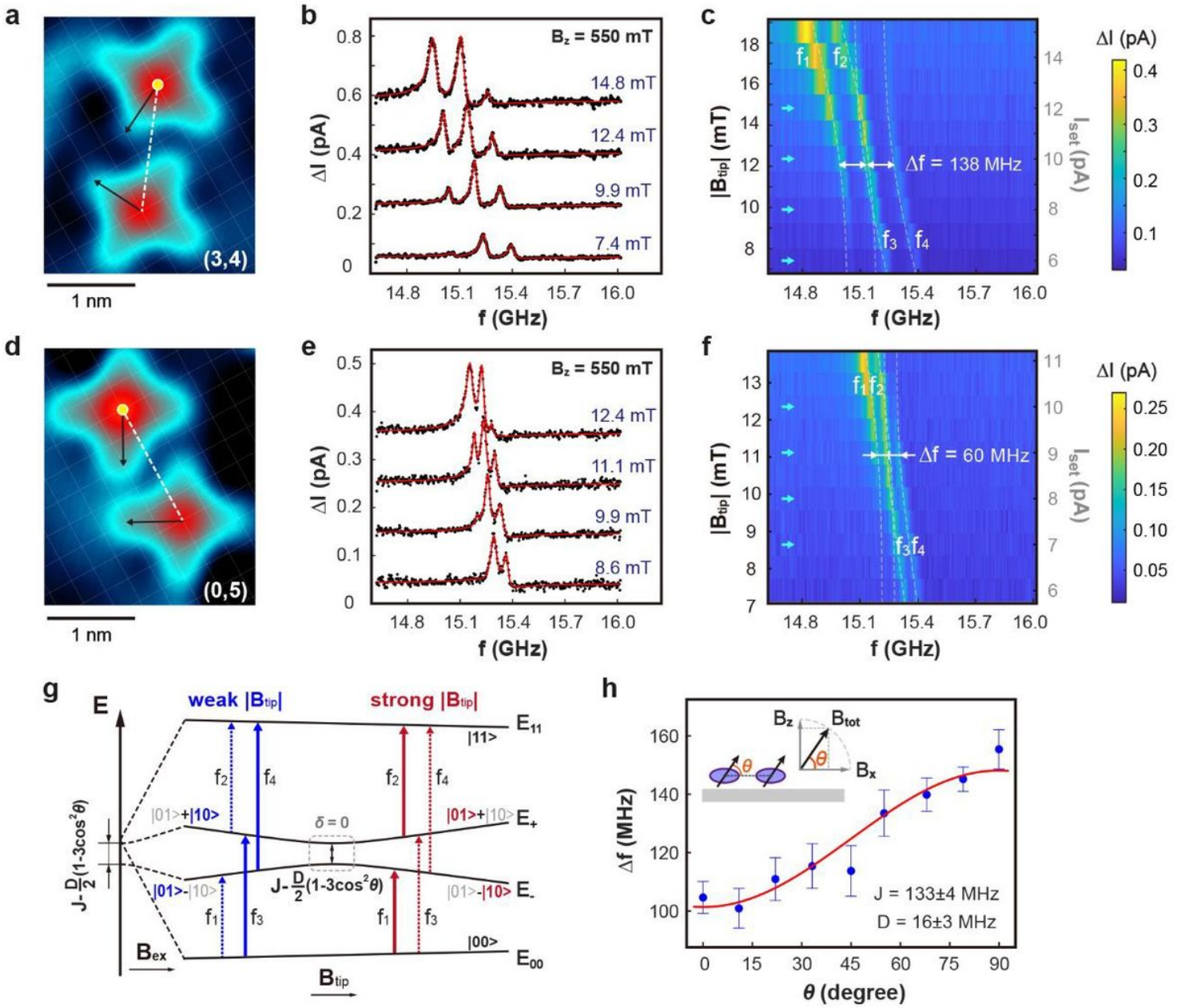

Figure 2

Spin coupling in FePc-FePc dimers. a, d, STM images of (3, 4) and (0, 5) dimer sharing the same center-center distance (dashed lines). Scanning conditions: V = 180 mV, Iset = 20 pA. b, e, Representative ESR spectra of the upper FePc measured at yellow dots in (a) and (d), respectively. c, f, ESR spectra plotted in color scale measured at different ⍰tip (⍰set). Blue arrows indicate each ESR spectrum presented in (b) and (e). The dotted white curves represent fitted ESR transitions. g, Energy level diagram of a two-spin system considering exchange (⍰) and dipolar (⍰) interaction in the presence of ⍰ex and ⍰tip. h, Measured (blue dots) and fitted (red curve) ESR splitting Δ⍰ of a (3, 4) dimer while rotating the external field by θ with

respect to the sample plane. Error bars denote the 95% confidence intervals. The total external field |⃗tot| was kept at 550 mT during the field rotation. All ESR spectra were taken with the same tip and V = 100 mV. (a)-(f) were obtained with an out-of-plane field of ⃗z = 550 mT. Vrf was set as 50 mV for (b)(c)(h) and 40 mV for (e)(f). ESR spectra of the lower FePc in each dimer are provided in Supplementary Fig. S4.

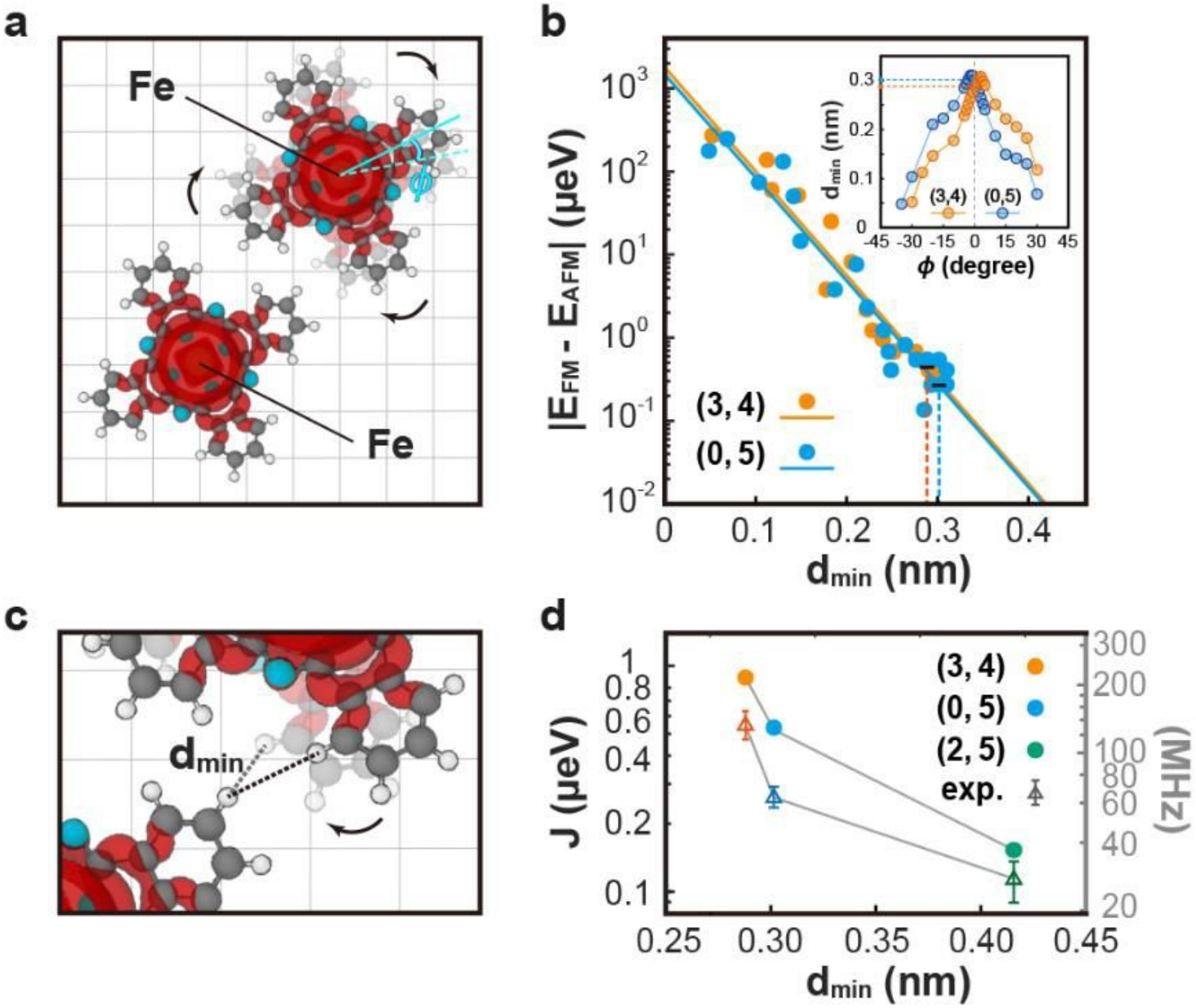

Figure 3

DFT calculations of exchange coupling in FePc-FePc dimer. a, Computational model of a FePc-FePc dimer. Fe-Fe distance is set according to experimental Fe coordinates. One molecule is fixed while the other one is rotated around the Fe center by ⃗. The minimum distance between two close-by ligands is denoted as ⃗min and amplified in (c). b, Calculated energy difference between FM and AFM coupling as a function of dmin for (3, 4) (orange dots) and (0, 5) (blue dots). Solid lines are fits based on |⃗FM−⃗AFM| ⃗exp (−⃗min/⃗). Inset: ⃗minas a function of ⃗. The ⃗min of optimized (3, 4) and (0, 5) configurations and corresponding |⃗FM−⃗AFM| are highlighted by dashed lines. d, Comparison of calculated (dots) and

experimental (triangles) □ for three different dimer configurations. The experimental data shown here is only the exchange coupling energy after subtracting the dipolar coupling energy (17 MHz for the (3, 4) , (0, 5) configurations and 14 MHz for the (2, 5) configuration) from the mean ESR splitting Δ□. Error bars represent the standard deviation. ESR spectra of (2, 5) dimer are provided in Supplementary Fig. S4.

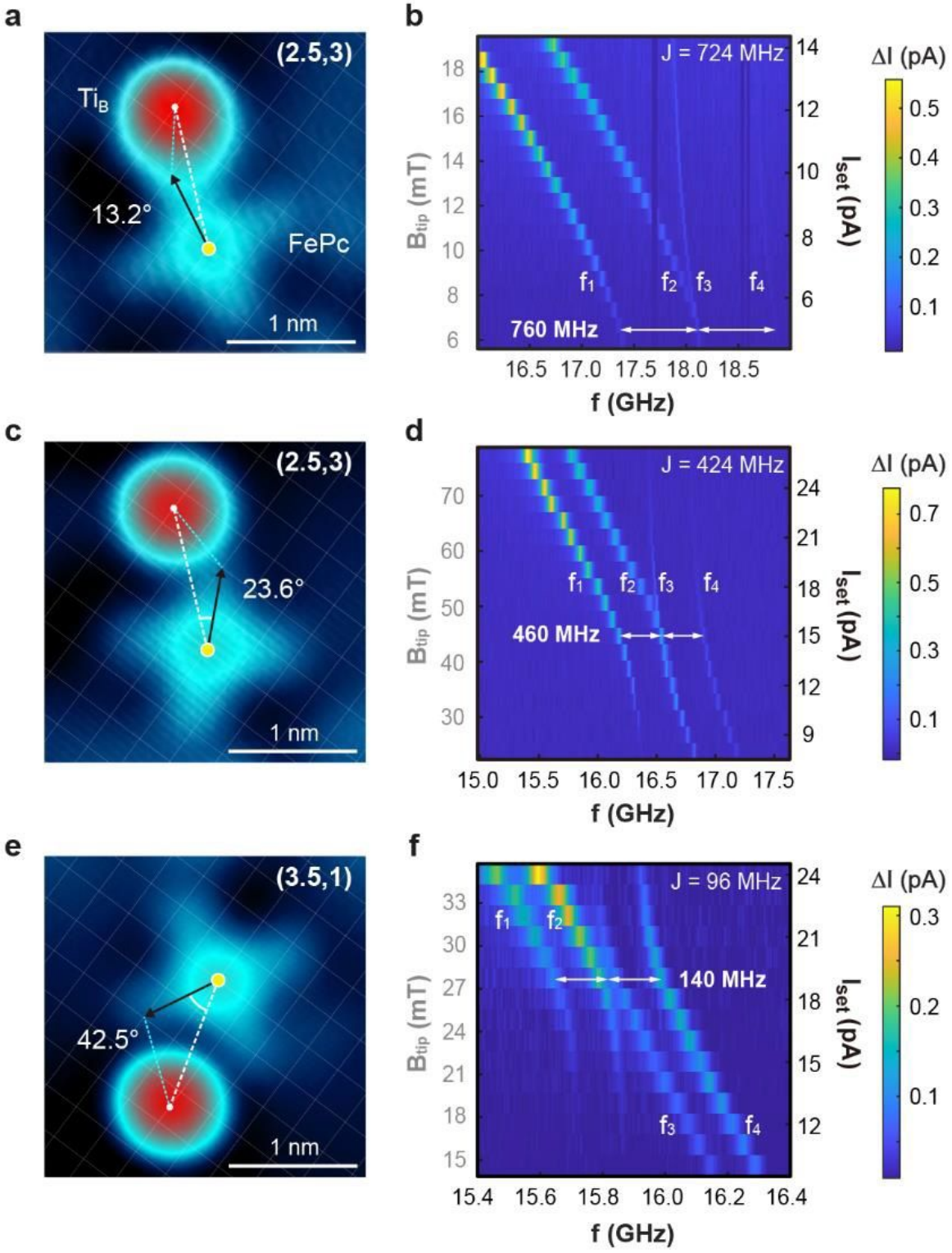

Figure 4

Exchange coupling of FePc-TiB pairs with different TiB-ligand distance. a, c, e, STM images of three FePc-TiB pairs with similar Fe-TiB distance but different angle between molecular axes and the connection of Fe-TiB. Scanning conditions: (a) V = 200 mV, Iset = 6 pA; (c) V = 200 mV, Iset = 10 pA; (e) V = 150 mV, Iset = 20 pA. b, d, f, Respective ESR spectra measured on FePc (yellow spots in (a)(c)(e)) as a function of tip field by varying setpoint of the tunneling current. The exchange coupling energy J of each FePc-TiB pair is labeled on the upper right corner, obtained by subtracting the dipolar coupling contribution (36 MHz for (2.5, 3) pair and 44 MHz for (3.5, 1) pair) from the measured ESR splitting. The external magnetic field was along out-of-plane direction for all FePc-TiB measurements in our work. ESR conditions: V = 100 mV for all three pairs and (b) Vrf = 30 mV, Bz = 650 mT, (d) Vrf = 10 mV, Bz = 600 mT, (f) Vrf = 30 mV, Bz = 570 mT.

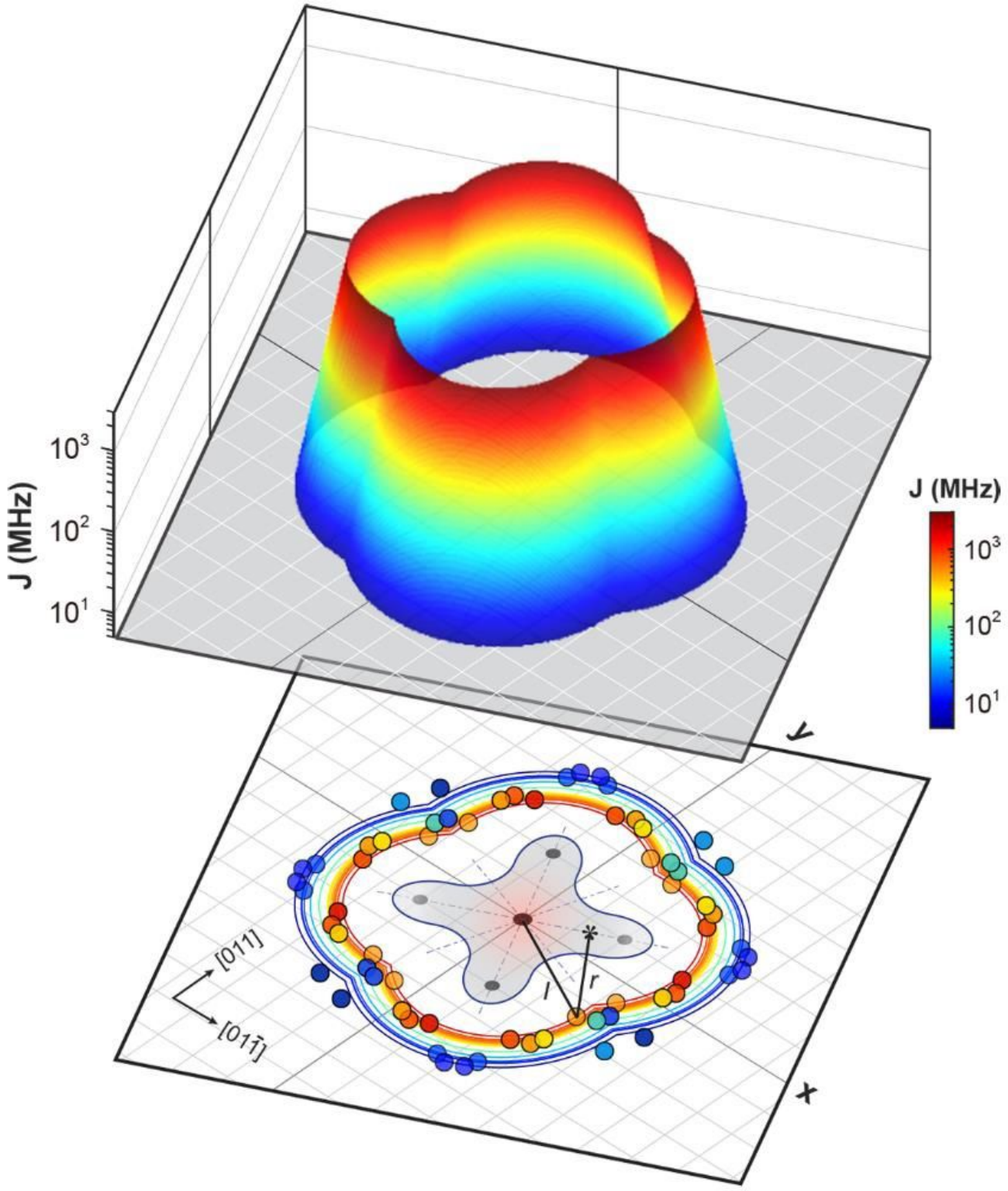

Figure 5

Anisotropic exchange coupling in FePc-TiB pairs. Lower panel: measured J of different FePc-TiB pairs expressed by colored dots and labelled at corresponding TiB adsorption sites with respect to the central FePc model. In total, 14 pairs were measured and the data points corresponding to the measured J have been equivalently duplicated by a rotation and reflection process according to the molecular symmetry axes (dashed lines). The grey grids represent the oxygen lattice. J is the exchange coupling energy after

subtracting the dipole contribution from the total ESR splitting. The contour lines are projected from the simulated spatial exchange coupling energy map choosing those J values obtained from the experiment. Upper panel: simulated spatial exchange coupling energy map by using a sum of two exponential terms representing □-dependence and □-dependence, respectively. The frequency range is set as 3,000 MHz (upper limit) and 5 MHz (lower limit).

Supplementary Files

This is a list of supplementary files associated with this preprint. Click to download.

- SI20201222submission.pdf